Ultra-high temperature ablation behavior of MoAlB ceramics under an oxyacetylene flame

Bei, Guoping; van der Zwaag, Sybrand; Kota, Sanklap; Barsoum, Michel W.; Sloof, Willem G.

DOI
10.1016/j.jeurceramsoc.2019.01.016

Publication date
2019

Document Version
Final published version

Published in
Journal of the European Ceramic Society

Journal of the European Ceramic Society 39 (2019) 2010–2017

Contents lists available at ScienceDirect

Journal of the European Ceramic Society

journal homepage: www.elsevier.com/locate/jeurceramsoc

Original Article

Ultra-high temperature ablation behavior of MoAlB ceramics under an oxyacetylene flame

Guoping Bei[a,*], Sybrand van der Zwaag[b], Sanklap Kota[c], Michel W. Barsoum[c], Willem G. Sloof[a]

[a] Department of Materials Science and Engineering, Delft University of Technology, Delft, Mekelweg 2, 2628 CD, Delft, the Netherlands
[b] Novel Aerospace Materials Group, Faculty of Aerospace Engineering, Kluyverweg 1, 2629 HS, Delft, the Netherlands
[c] Department of Materials Science & Engineering, Drexel University, Philadelphia, PA, 19104, USA

ARTICLE INFO

Keywords:
MoAlB
Ultra-high temperature ceramics
Ablation
High temperature oxidation
Oxyacetylene flame

ABSTRACT

The ultra-high temperature ablation of a polycrystalline, fully dense, predominantly single phase MoAlB ceramic discs under an oxyacetylene flame is examined. The linear ablation rate decreases from 1.3 μm/s during the first 30 s to - 0.7 μm/s after 60 s when the surface temperature reached about 2050 °C (with a flame temperature around 3000 °C). Up to 60 s, the MoAlB is ablation resistant due to the formation of a protective and viscous surface Al_2O_3 layer. As the ablation time is prolonged, the protective Al_2O_3 scale becomes porous and is almost fully destroyed at the central ablation region after 120 s. This accelerates the formation of large amounts of volatile species (mainly B and Mo oxides), resulting in a reduction in the ablation resistance.

1. Introduction

Ultra-high temperature ceramics (UHTCs) are a family of compounds that exhibit a unique set of properties, such as an extremely high melting point (beyond 3000 °C), a high chemical stability and an appreciable mechanical strength at high temperatures [1–5]. UHTCs are potential candidates for numerous high-temperature structural applications including thermal protection materials on hypersonic aerospace vehicles, re-usable atmospheric re-entry vehicles, specific components for propulsion, and nose cone and airframe leading edges [1–5]. However, only a limited number of ceramics and composites made of refractory metal borides, carbides, nitrides and oxides can survive in such extreme environments [1,2]. Among these UHTCs are borides and/or carbides of silicon, zirconium, hafnium, tantalum and composites thereof [5–11], which are characterized by high melting temperatures, high hardness values and excellent thermal conductivities. However, technological difficulties in manufacturing, including densification and machining into complex shapes, as well as their intrinsic brittleness and poor oxidation resistance have impeded their application.

Silicon carbide, SiC, is often added to borides to enhance their oxidation resistance by promoting the formation of a borosilicate-based glassy protective layer, which inhibits oxidation at temperatures up to 1700 °C for short times [1,2]. Recently, Ti_2AlC, a ternary carbide belonging to the family of MAX phases [12–14], where M is an early transition metal, A is an A group (mostly groups 13 and 14) element, and X is either carbon and/or nitrogen, showed promising ultra-high temperature properties because of the formation of an adherent Al_2O_3 protective surface layer [15]. Under an oxyacetylene flame at temperatures up to a flame temperature of 3000 °C, its linear ablation rate decreased from 0.14 μm/s for the first 30 s ablation to 0.08 μm/s after 180 s. Similarly, in situ formed Ti_3SiC_2 MAX phase particles in a C/SiC composite improved the ablation resistance of the latter due to the formation of protective SiO_2 and TiO_2 surface layers [16].

More recently, the ternary, atomically laminated boride, MoAlB, which has a crystal structure similar to that of MAX phases, has attracted quite some attention [17–23]. The crystal structure is orthorhombic and consists of MoB layers interleaved by two pure Al layers. With a Vickers hardness value ranging from 9 to 14 GPa, its hardness is quite a bit lower than typical binary transition metal borides [19,24–26], but, at about 2 GPa, the room temperature ultimate compressive strength of dense, 90 vol.% pure MoAlB ceramic is quite high [19]. The oxidation resistance of MoAlB is comparable to that of Al-containing MAX phases which form protective alumina, Al_2O_3, layers [27,28], such as, Ti_2AlC [29,30], Ti_3AlC_2 [31] and Cr_2AlC [32,33]. Oxidation of MoAlB at temperatures up to 1350 °C in air resulted in the formation of a dense and adherent Al_2O_3 scale. After 200 h at 1350 °C, the Al_2O_3 scale was only 25 μm thick. The growth of this protective oxide layer followed an approximately cubic time dependence [19,23]. The thermal shock behaviour of MoAlB ceramic [34] is comparable with that of MAX phases [35]. However, after quenching MoAlB with an initial strength of 307 MPa from 1400 °C into water, the residual

* Corresponding author.
E-mail address: G.Bei@tudelft.nl (G. Bei).

https://doi.org/10.1016/j.jeurceramsoc.2019.01.016
Received 5 December 2018; Received in revised form 7 January 2019; Accepted 9 January 2019
Available online 11 January 2019
0955-2219/

strength was about 45 MPa. Compared with MAX phases, MoAlB lacks multiple fracture energy absorbing mechanisms and the ability of healing crack damage. MoAlB also maintained a high and nearly temperature independent thermal conductivity (> 25 W/m/K) as well as a high Young's modulus of 319 GPa up to 1200 °C.

Although MoAlB is not an ultra-high temperature ceramic since it incongruently melts into the binary MoB and liquid Al above 1435 °C [22]. As noted above, it shows good oxidation as well as ablation resistance at high temperatures.

In the present work, the ablation behavior of spark plasma sintered (SPS) MoAlB ceramics exposed to an oxyacetylene flame with a flame temperature of around 3000 °C is investigated as a function of exposure time. The resulting compositional and microstructural changes are analyzed, and the ablation mechanisms are evaluated in conjunction with some thermodynamic calculations.

2. Experimental details

To fabricate dense MoAlB samples using SPS, MoAlB powder with an average particle size of about 38 μm, was used as the starting material. Full details of the synthesis of this powder have been reported in [19]. In brief, a powder mixture of molybdenum monoboride (MoB, 99%, Alfa Aesar, particle size < 44 μm) and aluminum (Al, Alfa Aesar, 99.5%, particle size < 38 μm) with a molar ratio of 1:1.3 was homogeneously mixed, cold-pressed and pressure-less sintered at 1000 °C for 15 h under a flowing Ar atmosphere. The MoAlB powder was placed between graphite punches in a graphite die (ISO-68, Toyo Tanso, Japan) with an inner diameter of 20 mm. Graphite foils (Papyrex Mersen, France) were used to prevent possible reactions between the powder and the graphite die and punches. In addition, these graphite foils were sprayed with BN on both sides for easy removal of the sample.

The powder mixture was then processed in an SPS installation (HP D 25 SD, FCT system GmbH, Germany) at 1250 °C for 0.5 h. The applied pressure was 50 MPa applied from the beginning of heating cycle. The furnace was flushed with pure Ar (5 N, Linde, The Netherlands). Heating and cooling rates were about 50 °C/min. The sample temperature was monitored using an axial pyrometer. The electric current was applied following a 15/5 (on/off 3 ms) pulse sequence. Finally, after releasing the pressure, the material was cooled from the sintering temperature to room temperature.

Electrical discharge machining was used to machine a 2 mm thin disk with a diameter of 20 mm. The disk was then cut into four quarters, which were in turn ground using SiC emery paper starting with 800 grit and finishing with 4000 grit. Finally, the ground surfaces were polished with 1 μm diamond suspension on a soft cloth. After each polishing step, the samples were ultrasonically cleaned in isopropanol and dried by blowing with pure nitrogen, N_2, gas (5 N, Linde, The Netherlands).

The ablation experiments were performed in accordance with the standard protocol for measuring the ablation properties of materials (GJB 323A-96) [9,15,36–38] exposed to an oxyacetylene flame. The pressure and the flow rate of acetylene were 0.095 MPa and 1.116 $m^3 h^{-1}$, respectively. The pressure and flow rates of oxygen were fixed to 0.4 MPa and 1.513 $m^3 h^{-1}$, respectively. The air-fuel equivalence ratio (λ) was 0.96; i.e. close to stoichiometric gas mixture composition. Under these conditions, according to the literature the flame can reach a temperature of about 3000 °C [9,15,36–38]. The actual flame temperature in our experiments was also measured with a Raytek Marathon MR1SCCF Pyrometer (Santa Cruz, CA, USA) having an accuracy of about ± 10 °C. For the conditions used, a flame tip temperature of 2800 ~ 3000 °C was measured. The distance between the stationary flame nozzle and sample surface was set at 10 mm. The flame centre and torch were aligned perpendicular to the sample surface. The torch was applied for 30, 60, 120 or 180 s. Also, the surface temperature of the MoAlB sample surface was measured with the Raytek Marathon MR1SCCF Pyrometer. The sample surface temperature reached up to 2050 ± 200 °C within 30 s. Towards the end of the 180 s ablation experiment, the sample surface temperature decreased by about 50 °C. This temperature decrease is due to microstructural and phase evolutions (See below). Upon prolonged ablation the formation of volatile phases results into heat loss which decreases the ablation temperature.

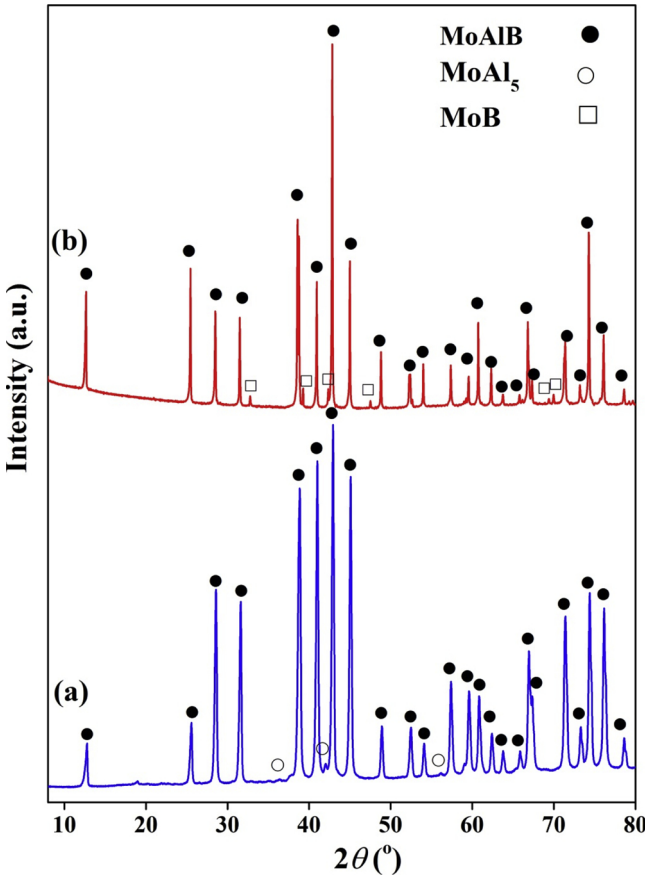

Fig. 1. X-ray diffractograms of (a) as received MoAlB powder, and (b) densified by SPS.

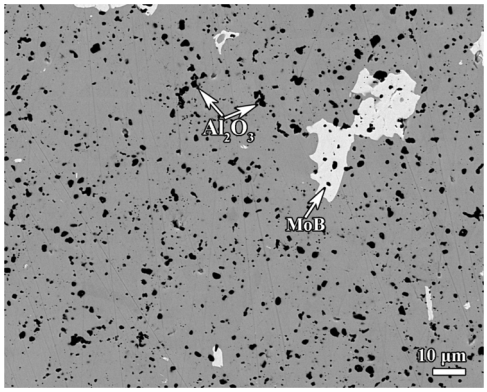

Fig. 2. SEM backscattered electron image of pristine MoAlB sample fabricated by SPS.

The mass ablation rate (R_m) and linear ablation rate (R_d) are defined, respectively, as:

$$R_m = \frac{m_t - m_0}{t} \quad (1)$$

$$R_d = \frac{d_t - d_0}{t} \quad (2)$$

where m_0 and m_t are the sample mass before and after ablation, respectively; d_0 and d_t denote the sample thickness of at the center of the

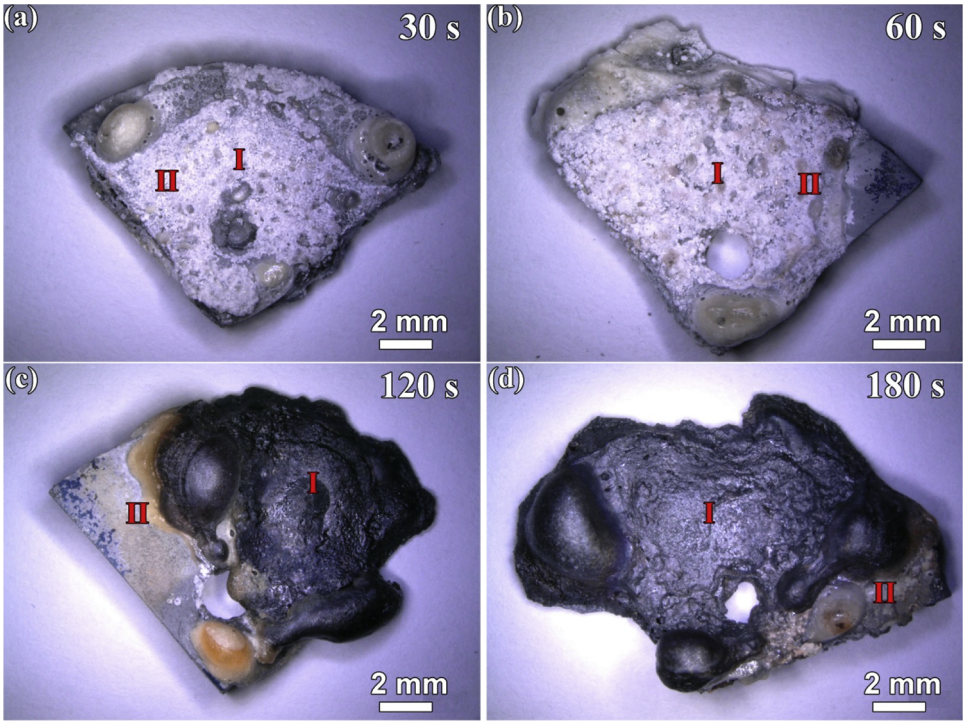

Fig. 3. Photographs of ablated MoAlB sample after exposure to an oxyacetylene flame for: (a) 30, (b) 60, (c) 120, and (d) 180 s. Area I: central ablation region, Area II: near central ablation region.

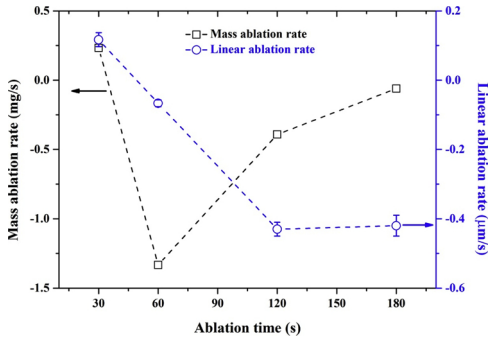

Fig. 4. Ablation rates of MoAlB sample as a function of ablation time. Left vertical-axis plots the mass ablation rate and the right vertical-axis, the linear ablation rate.

Table 1
Ablation properties of several high temperature ceramics and composites.

Materials	Ablation time (s)	Mass ablation rate (mg/s)	Linear ablation rate (μm/s)	References
MoAlB	30	0.23	1.3	This work
	60	−1.3	−0.7	
Ti_2AlC	60	−0.24	0.11	[15]
Cr_2AlC	60	13	44	[35]
ZrC/Cr_2AlC	60	45	2.5	
$C/C\text{-}SiC\text{-}Ti_3SiC_2$ composite	20	6.3	24	[7]
C/C-SiC composite	20	10.3	42	
BN-MAS composites	30	25.4	87	[9]

disks before and after ablation, respectively; *t* is the ablation time. Note these ablation rates are exposure time averaged values.

The phases present before and after ablation were identified with X-Ray diffraction (XRD) analysis using a Bruker D8 Advance diffractometer operated with Cu Kα radiation. Diffractograms were recorded in the 2θ range of 10–80° with a step size of 0.034°, and a counting time of 1 s per step. The ablated samples (with 120 s and 180 s ablation time) were crushed into a powder for the XRD analysis to avoid specimen height variation errors during the XRD scans. The diffractograms were evaluated using the Bruker Diffrac EVA software (Version 3.1).

The microstructure prior and after ablative testing was imaged in a scanning electron microscope (SEM) using a JSM 6500 F (JEOL, Japan) equipped with an energy dispersive spectrometer (EDS, Thermo-Noran, UltraDry, USA) for X-ray micro analysis (XMA). The volume fractions of the phases present were determined from the SEM micrographs by image analysis (ImageJ software, version 1.49, National Institute of Health, USA).

The chemical and phase reactions during the ablation process were evaluated in conjunction with thermodynamic calculations using FactSage software (version 7.1) [39]. The Gibbs free energy balance of various oxidation reactions of MoAlB in air was evaluated. The thermodynamic data of the oxidation products such as Al_2O_3, MoO_2 and MoO_3 as well as boron oxides (BO, B_2O_3) were taken from the FToxide database. The thermodynamic data of metallic Al and Mo were taken from Bins database [39]. The MoAlB phase was created with the thermodynamic data from [22]. For the phase diagram of MoAlB-O system, a gas mixture of Ar and O_2 with increasing oxygen partial pressure (in atm.) was considered to be in equilibrium with the different oxides as well as some precipitated phases.

3. Results and discussion

3.1. Ablation behaviour

In the as-received powder, in addition to the dominant MoAlB phase a minor fraction of $MoAl_5$ was also present; see Fig. 1(a). After densification by SPS, the MoAlB phase remained the dominant phase, while weaker diffraction lines indicate the presences of some β-MoB (PDF Card: 00-006-0644); see Fig. 1(b). In addition to these phases, a minor amount of Al_2O_3 was also observed in the SEM micrographs; see Fig. 2. The phase formation of β-MoB and Al_2O_3 may be due to minor oxidation of MoAlB during the SPS process. The volume fractions of the Al_2O_3

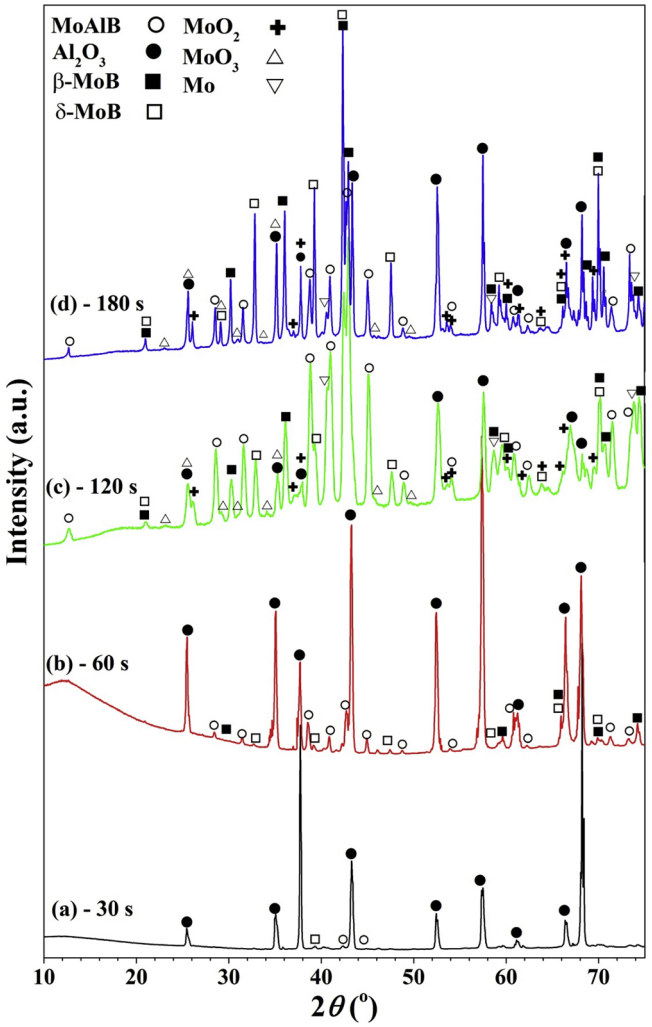

Fig. 5. X-ray diffractograms of ablated MoAlB sample after being exposed to oxyacetylene flame for: (a) 30, (b) 60, (c) 120, and (d) 180 s.

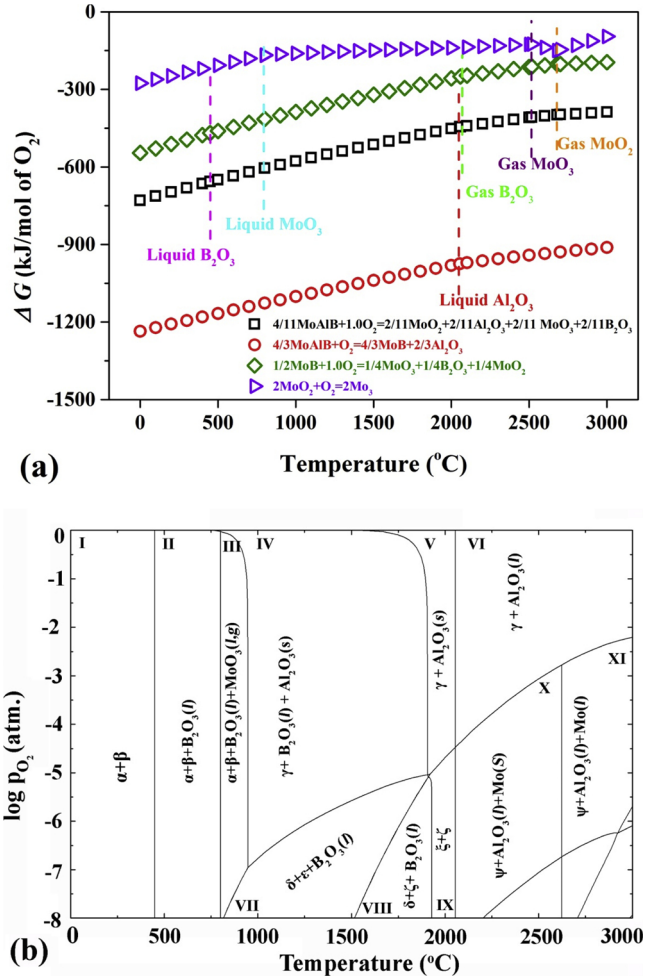

Fig. 6. Thermodynamic calculations: (a) Standard Gibbs free energy of various possible oxidation reactions of MoAlB, and (b) Phase diagram of the MoAlB-O system as a function of oxygen partial pressure (p_{O_2}) in the 0–3000 °C temperature range.

and MoB phases in the fully dense sample as determined by image analysis were 7 ± 1 and 3 ± 1 vol.%, respectively.

Fig. 3 shows images of the exterior surfaces of the MoAlB samples after exposure to the oxyacetylene flame for different times. After 30 s (Fig. 3(a)) and 60 s (Fig. 3(b)) ablation, the sample's overall shape did not change much. The entire surface is covered with a white layer identified as Al_2O_3; see below. Some material had melted at the edges of the ablated samples, and some large bubbles were observed. After longer ablation times, viz. 120 s (Fig. 3(c)) and 180 s (Fig. 3(d)), the sample surface turned black. Furthermore, a significant amount of material appeared to have flown to the edges of the ablated samples, thereby changing their shape. Here again, many large and small bubbles were observed.

The ablation behaviour is quantified using the time averaged linear and mass ablation rates (cf. Eqs. (1) and (2)) as a function of time and the results are shown in Fig. 4. The mass ablation rate, $R_{m,}$ (left vertical-axis in Fig. 4) was about 0.23 mg/s for the initial 30 s, which indicates that the oxidation induced mass gain was higher than the material loss at this stage. However, after 60 s, R_m is negative (-1.3 mg/s). The change in sign implies that the sample lost weight most likely due to the formation and volatilization of B and Mo oxides [23] as well as scouring of the Al_2O_3 layer formed by the high-velocity gas flame. Upon further ablation, R_m increased slightly towards smaller, but still negative values (-0.06 mg/s). This may be due to complex solid-liquid-gas reactions that occur during the ablation process. The evaporation of volatile species and the flow of liquid phases may have reduced the surface temperature and consequently reduced R_m.

The linear ablation rate, R_d, (right axis in Fig. 4) decreased monotonically with time. For the initial 30 s and 60 s, the R_d were 0.12 ± 0.02 and - 0.07 ± 0.01 μm/s, respectively. This indicates that the shape of the MoAlB ceramic hardly changed and the material can withstand the hot corrosion in the ablation process up to 60 s. However, after 120 and 180 s of ablation, R_d was significantly reduced to -4.30 ± 0.03 and -4.20 ± 0.02 μm/s, respectively. This is due to a significant change of the sample shape at the central ablation region due to the hot corrosion; see Fig. 3(c) and (d).

The MoAlB ablation rates and those of other ultra-high temperature monolithic ceramics and related composites tested under similar oxyacetylene flame conditions are listed in Table 1. The low ablation rate of MoAlB, at least during the first 60 s, indicates that it exhibits excellent ablation behaviour, making it a promising material for ultra-high temperature applications.

3.2. Phase composition and ablation reactions

The phase composition of the ablated MoAlB surfaces changed with ablation time. After the initial 30 s ablation, strong diffraction lines of only α-Al_2O_3 (Corundum, PDF card: 00-010-0173) were observed, while weak diffraction lines of MoAlB and MoB (β-MoB, PDF Card: 00-006-0644) were detected; see Fig. 5(a). It follows that the white layer covering the surface (Fig. 3(a)) is mainly comprised of Al_2O_3 and is relatively thick. Extending the ablation time to 60 s increased the

Table 2
Phases in the MoAlB-O system in the temperature range of 0–3000 °C and oxygen partial pressures between 10^{-8} and 1 atm.

	Solid phase	Liquid phase	Gas phase
I	α (B_2O_3 + Al_2O_3 + MoO_3)	–	β (Ar + O_2)
II	α (B_2O_3 + Al_2O_3 + MoO_3)	B_2O_3	β (Ar + O_2)
III	α (B_2O_3 + Al_2O_3 + MoO_3)	B_2O_3 + MoO_3	Ar + O_2 + MoO_3
IV	Al_2O_3	B_2O_3	γ(Ar + O_2 + MoO_3 + B_2O_3)
V	Al_2O_3	–	γ (Ar + O_2 + MoO_3 + B_2O_3)
VI	–	Al_2O_3	γ(Ar + O_2 + MoO_3 + B_2O_3)
VII	ε(Al_2O_3 + MoO_2)	B_2O_3	δ(Ar + MoO_3 + B_2O_3)
VIII	ζ(Al_2O_3 + Mo)	B_2O_3	δ(Ar + MoO_3 + B_2O_3)
IX	ζ(Al_2O_3 + Mo)	–	ξ (Ar + MoO_3 + MoO_2 + BO + B_2O_3)
X	Mo	Al_2O_3	ψ(Ar + Al + MoO_3 + MoO_2 + BO + B_2O_3)
XI	–	Al_2O_3 + Mo	ψ(Ar + Al + MoO_3 + MoO_2 + BO + B_2O_3)

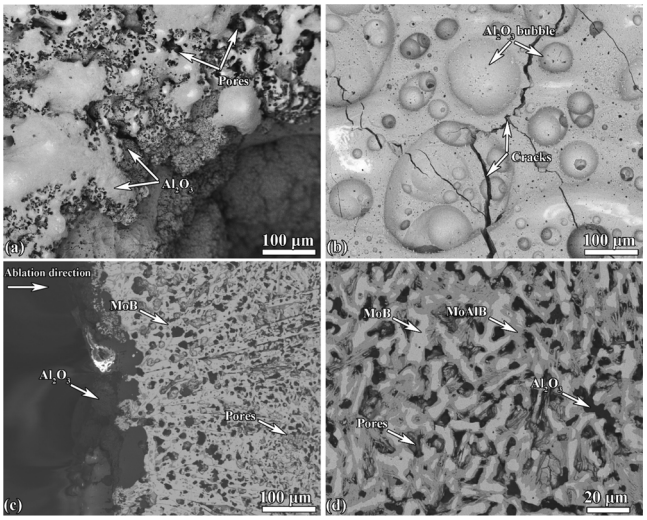

Fig. 7. SEM backscattered electron images of the MoAlB sample after 30 s ablation: (a) central ablation region, (b) near the central ablation region, (c) cross section of the central ablation region, and (d) inner part of the cross section.

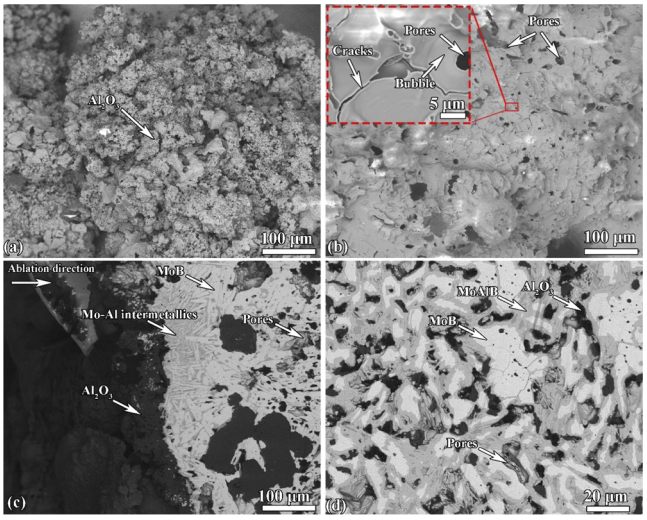

Fig. 8. SEM backscattered electron images of the MoAlB sample after 60 s ablation: (a) central ablation region, (b) near central ablation region. Inset: enlarged SEM images of red rectangle showing evidence for volatile oxidation products escaping from the viscous Al_2O_3 layer, (c) cross section at the central ablation region, and (d) inner part of the cross section. (For interpretation of the references to colour in this figure legend, the reader is referred to the web version of this article).

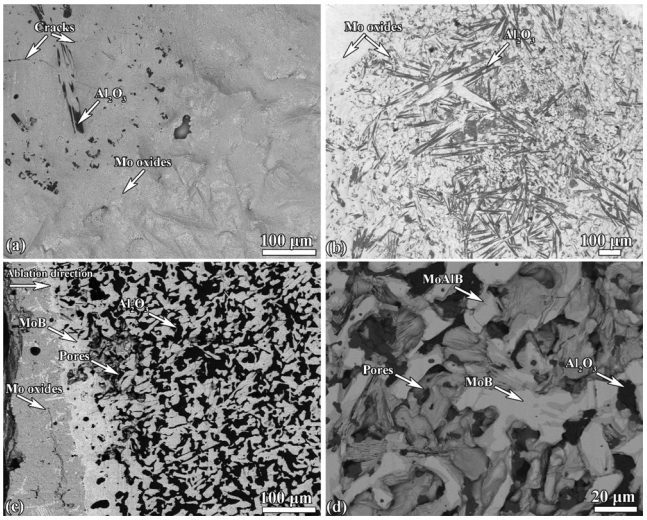

Fig. 9. SEM backscattered electron images of the MoAlB sample after 120 s ablation: (a) central ablation region, (b) near central ablation region, (c) cross section under the central ablation region, and (d) higher magnification of the inner part of the section.

intensity of the MoAlB and MoB diffraction lines(Fig. 5(b)), suggesting the thick Al_2O_3 surface layer started to erode. The phase compositions after 120 s and 180 s (Fig. 5(c) and (d)) are similar to each other. In both cases, with increased ablation time, in addition to the diffraction lines belonging to α-Al_2O_3, the diffraction lines of the MoB phases (β-MoB, PDF Card: 00-006-0644 and δ-MoB, PDF Card: 04-007-1330) became stronger and those of the MoAlB phase became weaker. Furthermore, diffraction lines of Mo oxides, MoO_2, (Tugarinovite, PDF Card:04-007-2356) and MoO_3 (PDF Card: 00-047-1081)) were detected indicating that more Mo oxides were formed at later stages of the ablation process. Interestingly, after 120 s and 180 s ablation, diffraction lines of metallic Mo were also present. Lastly, in all recorded XRD patterns, no diffraction lines corresponding to boron containing oxides were observed, suggesting that any boron oxide formed was either amorphous or had evaporated [22,23]. The evaporation of glassy B_2O_3 phase has been widely observed in the ablation of di-borides, such as HfB_2 and ZrB_2 [2].

Despite the high temperatures, high pressures and high velocity combustion gases generated under an oxyacetylene flame, it appears that MoAlB endures a combination of thermal, chemical, physical and mechanical actions. A series of reactions also occur between the ultra-high temperature oxidative gas species and MoAlB. Based on our XRD analysis, our thermodynamic calculations and the reported oxidation mechanism of MoAlB [22,23], the following reactions are assumed to take place during the ablation process:

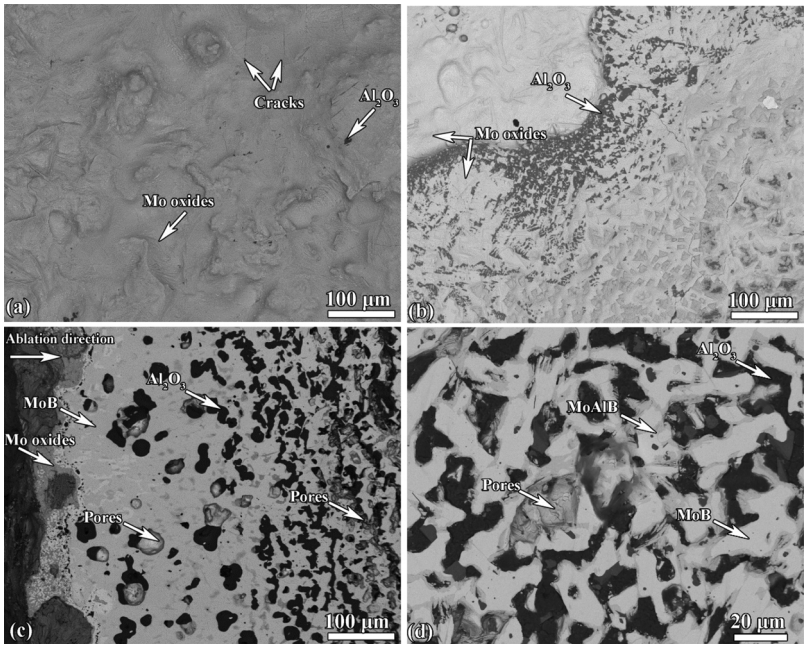

Fig. 10. SEM backscattered electron images of the MoAlB sample after 180 s ablation: (a) central ablation region, (b) near central ablation region, (c) cross section at the central ablation region, and (d) higher magnification of the inner part of the section.

$$\frac{4}{3}MoAlB(s,\ l) + O_2 \rightarrow \frac{4}{3}MoB + \frac{2}{3}Al_2O_3 \tag{3}$$

$$\frac{4}{11}MoAlB(s) + O_2(g) \rightarrow \frac{2}{11}Al_2O_3(s,\ l) + \frac{2}{11}MoO_3(s,\ l,\ g) + \frac{2}{11}B_2O_3(s,\ l,\ g) + \frac{2}{11}MoO_2(s,\ l,\ g) \tag{4}$$

$$\frac{1}{2}MoB(s) + O_2(g) \rightarrow \frac{1}{4}MoO_2(s,\ l) + \frac{1}{4}B_2O_3(l,\ g) + \frac{1}{4}MoO_3(s,\ l,\ g) \tag{5}$$

$$2MoO_2(s,\ g) + O_2 \rightarrow 2MoO_3(s,\ g,\ l) \tag{6}$$

$$3MoO_2(s,\ g) \rightarrow 2MoO_3(l,\ g) + Mo(s,\ l) \tag{7}$$

Here *s*, *l*, and *g* denote *solid*, *liquid* and *gas*, respectively. From the thermodynamic calculations of the various oxidation reactions (see Fig. 6(a)), the formation of Al_2O_3 according to Eq. (3) prevails. This is in good agreement with our XRD analysis of the material after 30 s ablation; see Fig. 5(a). Upon prolonged ablation, the formation of B_2O_3 (melting point: 486 °C) and Mo oxides, such as MoO_2 and MoO_3 (melting point: 801 °C), may develop according to reactions Eqs.(4) and (5). This is also consistent with the XRD analysis of the ablated surface after 120 and 180 s ablation; see Fig. 5(c) and (d).

Since ultra-high temperature ablation is a dynamic oxidative process, the oxygen partial pressure (p_{O_2}) plays an important role in the final formation of the oxidation products. The phase diagram of the MoAlB-O system as a function of p_{O_2} over the temperature range of 0–3000 °C is presented in Fig. 6(b) and the corresponding phases are listed in Table 2. This diagram indicates that $\alpha(B_2O_3 + Al_2O_3 + MoO_3)$ solid oxides may form when the temperature is below 486 °C. The glassy B_2O_3 phase becomes liquid at 486 °C and becomes gaseous when the temperature is above 797 °C; cf. Fig. 6(b) and Table 2. Furthermore, it will transform into a fully gaseous phase when the temperature exceeds 1990 °C; see section V. Concerning the MoO_3 phase, the liquid and gaseous MoO_3 phases are formed simultaneously at temperatures above 803 °C (see section III in Fig. 6(b)), while the liquid MoO_3 phase becomes fully gaseous at temperatures above 947 °C; see section IV in Fig. 6(b). The evolution of the gaseous MoO_3 phase has also been observed when oxidizing Mo in air at high temperatures [40,41]. The MoO_3 phase volatilizes by sublimation as it forms on Mo substrates. Thus, when the temperature rises above 1907 °C, large amounts of gaseous phases most probably consisting of MoO_3 and B_2O_3 evolve; see section V in Fig. 6(b). When the temperature exceeds 2053 °C, liquid Al_2O_3 will be formed; see section IV in Fig. 6(b).

when the temperature is beyond 947 °C, MoO_2 will be formed at p_{O_2} (between 10^{-8} and $10^{-2.3}$ atm.); see section VII in Fig. 6(b). This phase will either sublimate (see section IX, X and XI in Fig. 6(b)) or undergo complex oxidation and decomposition reactions; see Eqs. (6) and (7)) [40,41]. These oxidation and decomposition reactions result in the formation of the pure metallic Mo phase (*s, l*) and gaseous MoO_3 when the temperature is beyond 1637°C; see sections X and IX in Fig. 6(b).

The precipitation of Mo according to Eq. (7), agrees with the observed Mo phase detected after 120 and 180s ablation; see Fig. 5(c) and (d). Note this only happens, however, at lowp_{O_2}

In addition to the gaseous Mo oxides (MoO_3 + MoO_2) and B_2O_3, Al (*g*) and BO(g) can also be formed when the temperature is above 2057 and 2627°C, respectively, and the oxygen partial pressure is low, i.e. between 10^{-8} to $10^{-2.3}$ atm.; see section X and XI in Fig. 6(b).

3.3. Microstructure characterization and ablation mechanisms

The observed morphologies, microstructures and chemical compositions of the MoAlB surfaces change with ablation time. After 30 s of ablation, a porous Al_2O_3 layer (Fig. 7(a)) forms in the centre of the ablated region (region I in Fig. 5(a)). The pores are likely due to the high-speed gas flow. Near the edges of the ablated region (area II in Fig. 5(a)), a much denser Al_2O_3 scale in which some large bubbles are present was observed (Fig. 7(a)). These bubbles are probably due to the release of volatile oxidation products [42]. As noted above, exposure of the MoAlB samples to such harsh high-temperature conditions leads to the formation of volatile Mo oxides (MoO_2 and MoO_3) and boron oxides (BO and B_2O_3). These volatile oxides are presumably captured inside the viscous Al_2O_3 layer resulting in bubble formation. In this near central ablation region, many microcracks in the Al_2O_3 layer were also observed (Fig. 7(b)), whose presence is likely to be due to the mismatch in thermal expansion between the Al_2O_3 and the substrate upon final cooling from the ultra-high ablation temperature to room temperature.

However, underneath the porous Al_2O_3 layer, a mixture of MoB and Al_2O_3 was formed with many pores (see Fig. 7(c) and (d)) and almost no

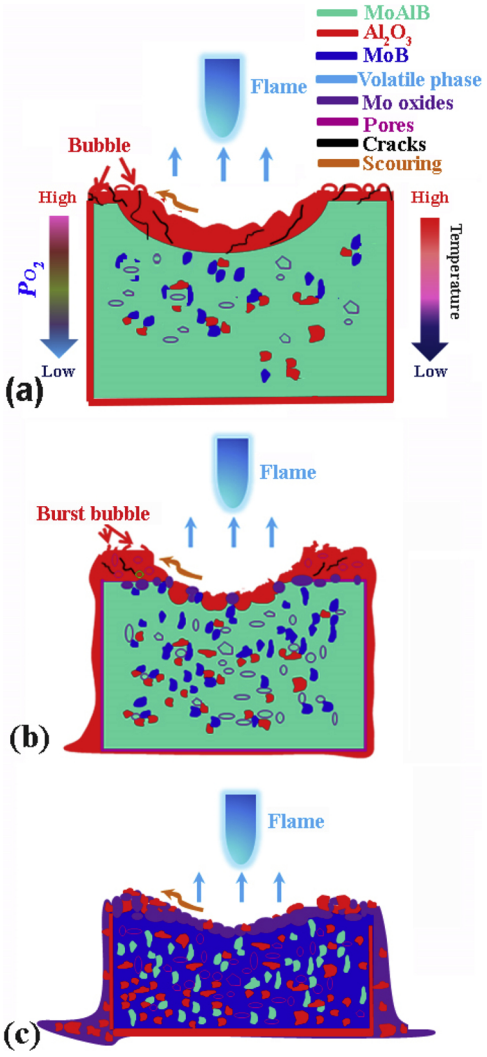

Fig. 11. Schematic representation of the ablation behavior of an MoAlB sample exposed to an oxyacetylene flame.

residual MoAlB phase was detected. When oxygen reacts with MoAlB according to Eq. (3), the formation of MoB and Al_2O_3 is expected. The remaining material consists of MoAlB with MoB and Al_2O_3, and a significant amount of pores.

Extending the ablation time to 60 s, the microstructure under the central ablation region is similar to that observed after 30 s (compare Figs. 7(a) and 8 (a)). However, near the central ablation region, this Al_2O_3 layer becomes quite porous; see Fig. 8(b). The bubbles seen after 30 s ablation likely burst due to the stronger volatilization of Mo and B oxides. Underneath the porous Al_2O_3 layer, in addition to MoB, a Mo-Al intermetallic phase was also observed; see Fig. 8(c). The Mo/Al atom ratio of this intermetallic phase is close to 2.6, which suggests it is Mo_3Al_8. The formation of this phase is either due to decomposition of the MoAlB phase at high temperatures [23], or due to the reaction between Mo(*s, g, l*) and Al(*g*). From the MoAlB-O phase diagram, we conclude that Mo(*s, l, g*) and Al(*g*) will be formed at oxygen partial pressures < 0.025 atm. The remaining material consists of MoAlB with MoB and Al_2O_3, and has a significant amount of porosity, while the amounts of MoB and Al_2O_3 are increased at the expense of MoAlB.

After prolonged ablation, i.e. up to 120 and 180 s, the central ablation region is comprised of mainly MoO_2 or/and MoO_3, and minor amounts of Al_2O_3; see Figs. 9(a)–(b) and 10 (a) - (b). The Mo oxides covering the surface melt and the protective Al_2O_3 layer for the most part no longer exists. It was either blown to the side of the ablation centre or evaporated; see Fig. 9(b) and 10 (b). The thickness of the Mo oxide layer reduces with ablation time; cf. Figs. 9(c) and 10 (c). Underneath the Mo oxide layers, the material consists of Mo or/and MoB and some Al_2O_3 as confirmed with X-ray microanalysis. The remaining material mainly consists of MoB with some MoAlB. Its structure is very porous; see Figs. 9(c) and 10 (c). Note the average pore size increases with ablation time; see Figs. 7(d), 8 (d), 9 (d) and 10 (d).

To summarize, a schematic representation of the ablation behaviour of MoAlB exposed to an oxyacetylene flame, is shown in Fig. 11. First, the MoAlB is eroded by a combination of fast heating and high thermal loads. Initially, a relatively thick Al_2O_3 layer is formed by oxidation of the MoAlB. Then, scouring of the Al_2O_3 layer, which turns viscous and consumes most of the heat input by the flame takes place and this reduces the high temperature erosion. This phenomenon offers early stage protection of the MoAlB matrix. Meanwhile, volatile gas species like Mo oxides and B_2O_3 are also generated. The latter are trapped beneath the viscous Al_2O_3 layer resulting in bubble formation near the central ablation area. Upon prolonged ablation the Al_2O_3 layer becomes more porous and less protective, leading to the formation of large amounts of volatile Mo oxide and B_2O_3; see Fig. 11(b). This, in turn, results in significant mass loss. Further ablation is accompanied by oxidation of the core of the MoAlB material, forming a mixture of porous MoB and porous Al_2O_3. At the final stage of the ablation process, almost all the Al_2O_3 is either evaporated or blown to the side of the central area and the surface is mainly covered with non-protective Mo oxides (MoO_2 and MoO_3); see Fig. 11(c).

Thus, to further improve the ablation behaviour of the MoAlB ceramic two different routes are proposed. Firstly, addition of a binary carbide such as SiC to manufacture SiC-MoAlB composites that would form a borosilicate glass layer [1] during the high temperature ablation process. Secondly, aligning the orientation of the MoAlB grains, like textured Ti_3AlC_2 [43], such that the formation of alumina upon high temperature ablation is promoted by fast diffusion of Al out of the orthorhombic crystal lattice.

4. Conclusions

The ablation of MoAlB exposed to an oxyacetylene flame is governed by thermal oxidation and scouring of the various oxidation products by the high-speed gas flow. The ternary MoAlB can survive ultra-high temperature ablation for the first 60 s due to the formation of a protective and viscous Al_2O_3 layer on its surface. The linear ablation rate decreases from 1.33 μm/s for the first 30 s to -0.69 μm/s after 60 s. However, after about 120 s of high-temperature ablation, the protective Al_2O_3 scale is practically lost. Then, the ablation is accelerated due to the formation of large amounts of volatile Mo oxides (MoO_2 and MoO_3) and B_2O_3.

Acknowledgments

Financial support from German Research Foundation (Deutsche Forschungsgemeinschaft, DFG, SPP 1568'Design and Generic Principles of Self-Healing Materials', SL184/1-2) and DFG Junior Project within the framework of the "Promotion of young researchers" in the SPP 1568 for Dr. Guoping Bei is gratefully acknowledged. The authors are grateful to Mr. Jurriaan van Slingerland for his help with the ablation experiments. Sanklap Kota and Michel W. Barsoum were funded by an NSF (1729335 DMR-REF) grant.

References

[1] E. Wuchina, E. Opila, M. Opeka, W. Fahrenholtz, I. Talmy, UHTCs: ultra-high temperature ceramic materials for extreme environment applications, Electrochem. Soc. Interface 16 (2007) 30–36.
[2] W.G. Fahrenholtz, G.E. Hilmas, Oxidation of ultra-high temperature transition metal diboride ceramics, Int. Mater. Rev. 57 (2012) 61–72, https://doi.org/10.1179/1743280411Y.0000000012.
[3] S.R. Levine, E.J. Opila, M.C. Halbig, J.D. Kiser, M. Singh, J.A. Salem, Evaluation of ultra-high temperature ceramics for aeropropulsion use, J. Eur. Ceram. Soc. 22 (2002) 2757–2767, https://doi.org/10.1016/S0955-2219(02)00140-1.
[4] S. Tang, J. Deng, S. Wang, W. Liu, K. Yang, Ablation behaviors of ultra-high

temperature ceramic composites, Mater. Sci. Eng. A 465 (2007) 1–7, https://doi.org/10.1016/j.msea.2007.02.040.
[5] X. Jin, X. Fan, C. Lu, T. Wang, Advances in oxidation and ablation resistance of high and ultra-high temperature ceramics modified or coated carbon/carbon composites, J. Eur. Ceram. Soc. 38 (2018) 1–28, https://doi.org/10.1016/j.jeurceramsoc.2017.08.013.
[6] M. Kazemzadeh Dehdashti, W.G. Fahrenholtz, G.E. Hilmas, Effects of transition metals on the oxidation behavior of ZrB_2 ceramics, Corros. Sci. 91 (2015) 224–231, https://doi.org/10.1016/j.corsci.2014.11.019.
[7] L. Xiang, L. Cheng, X. Fan, L. Shi, X. Yin, L. Zhang, Effect of interlayer on the ablation properties of laminated HfC–SiC ceramics under oxyacetylene torch, Corros. Sci. 93 (2015) 172–179, https://doi.org/10.1016/j.corsci.2015.01.021.
[8] H.J. Li, X.Y. Yao, Y.L. Zhang, K.Z. Li, L.J. Guo, L. Liu, Effect of heat flux on ablation behaviour and mechanism of C/C–ZrB_2–SiC composite under oxyacetylene torch flame, Corros. Sci. 74 (2013) 265–270, https://doi.org/10.1016/j.corsci.2013.04.052.
[9] D. Cai, Z. Yang, J. Yuan, X. Duan, S. Wang, V. Ocelik, D.I. Vainchteind, J.Th.M. de Hosson, D. Jia, Y. Zhou, Ablation behavior and mechanism of boron nitride - magnesium aluminum silicate ceramic composites in an oxyacetylene combustion flame, Ceram. Int. 44 (2018) 1518–1525, https://doi.org/10.1016/j.ceramint.2017.10.063.
[10] S.A. Chen, C. Zhang, Y. Zhang, D. Zhao, H. Hu, Z. Zhang, Mechanism of ablation of 3D C/ZrC–SiC composite under an oxyacetylene flame, Corros. Sci. 68 (2013) 168–175, https://doi.org/10.1016/j.corsci.2012.11.009.
[11] S. Zhou, W. Li, P. Hu, C. Hong, L. Weng, Ablation behavior of ZrB_2–SiC–ZrO_2 ceramic composites by means of the oxyacetylene torch, Corros. Sci. 51 (2009) 2071–2079, https://doi.org/10.1016/j.corsci.2009.05.035.
[12] M.W. Barsoum, The $M_{N+1}AX_N$ phases: a new class of solids thermodynamically stable nanolaminates, Prog. Solid State Chem. 28 (2000) 201–281, https://doi.org/10.1016/S0079-6786(00)00006-6.
[13] Z.M. Sun, Progress in research and development on MAX phases: a family of layered ternary compounds, Int. Mater. Rev. 56 (2011) 143–166, https://doi.org/10.1179/1743280410Y.0000000001.
[14] M.W. Barsoum, M. Radovic, Elastic and mechanical properties of the MAX phases, Annu. Rev. Mater. Res. 41 (2011) 195–227, https://doi.org/10.1146/annurev-matsci-062910-100448.
[15] G.M. Song, S.B. Li, C.X. Zhao, W.G. Sloof, S. van der Zwaag, Y.T. Pei, J.T.M. de Hosson, Ultra-high temperature ablation behavior of Ti_2AlC ceramics under an oxyacetylene flame, J. Eur. Ceram. Soc. 31 (2011) 855–862, https://doi.org/10.1016/j.jeurceramsoc.2010.11.035.
[16] X. Fan, X. Yin, L. Wang, L. Cheng, L. Zhang, Processing, microstructure and ablation behavior of C/SiC–Ti_3SiC_2 composites fabricated by liquid silicon infiltration, Corros. Sci. 74 (2013) 98–105, https://doi.org/10.1016/j.corsci.2013.04.029.
[17] W. Jeitschko, Die Kristallstruktur von MoAlB, Monatsh. Chem. Verw. Teile. Anderer.Wiss 97 (1966) 1472–1476, https://doi.org/10.1007/BF00902599.
[18] S. Okada, K. Iizumi, K. Kudaka, K. Kudou, M. Miyamoto, Y. Yu, T. Lundström, Single crystal growth of $(Mo_xCr_{1-x})AlB$ and $(Mo_xW_{1-x})AlB$ by metal Al solutions and properties of the crystals, J. Solid State Chem. 133 (1997) 36–43, https://doi.org/10.1006/jssc.1997.7313.
[19] S. Kota, E. Zapata-Solvas, A. Ly, J. Lu, O. Elkassabany, A. Huon, W.E. Lee, L. Hultman, S.J. May, M.W. Barsoum, Synthesis and characterization of an alumina forming nanolaminated boride: MoAlB, Sci. Rep. 6 (2016) 26475, https://doi.org/10.1038/srep26475.
[20] X. Li, H. Cui, R. Zhang, First-principles study of the electronic and optical properties of a new metallic MoAlB, Sci. Rep. 6 (2016) 39790, https://doi.org/10.1038/srep39790.
[21] Y. Bai, X. Qi, A. Duff, N. Li, F. Kong, X. He, R. Wang, W.E. Lee, Density functional theory insights into ternary layered boride MoAlB, Acta Mater. 132 (2017) 69–81, https://doi.org/10.1016/j.actamat.2017.04.031.
[22] S. Kota, M. Agne, E. Zapata-Solvas, O. Dezellus, D. Lopez, B. Gardiola, M. Radovic, M.W. Barsoum, Elastic properties, thermal stability, and thermodynamic parameters of MoAlB, Phys. Rev. B: Condens. Matter 95 (2017) 144108, , https://doi.org/10.1103/PhysRevB.95.144108.
[23] S. Kota, E. Zapata-Solvas, Y. Chen, M. Radovic, W.E. Lee, M.W. Barsoum, Isothermal and cyclic oxidation of MoAlB in air from 1100 °C to 1400 °C, J. Electrochem. Soc. 164 (2017) C930–C938, https://doi.org/10.1149/2.1891713jes.
[24] S. Okada, Synthesis, Crystal Structure and Characterizations of the Ternary Borides TMAlB (TM = Mo, W) with UBC Type Structure 31 Kokushikan Univ. Fac. Eng, 1998, http://iss.ndl.go.jp/books/R100000002-I000000008400-00.
[25] M. Ade, H. Hillebrecht, Ternary borides Cr2AlB2, Cr_3AlB_4, and Cr_4AlB_6: the first members of the series $(CrB2)_nCrAl$ with n = 1, 2, 3 and a unifying concept for ternary borides as MAB-phases, Inorg. Chem. 54 (2015) 6122–6135, https://doi.org/10.1021/acs.inorgchem.5b00049.
[26] L. Xu, O. Shi, C. Liu, D. Zhu, S. Grasso, C. Hu, Synthesis, microstructure and properties of MoAlB ceramics, Ceram. Int. 44 (2018) 13396–13401, https://doi.org/10.1016/j.ceramint.2018.04.177.
[27] D.J. Tallman, B. Anasori, M.W. Barsoum, A critical review of the oxidation of Ti_2AlC, Ti_3AlC_2 and Cr_2AlC in air, Mater. Res. Lett. 1 (2013) 115–125, https://doi.org/10.1080/21663831.2013.806364.
[28] X.H. Wang, Y.C. Zhou, Layered machinable and electrically conductive Ti_2AlC and Ti_3AlC_2 ceramics: a review, J. Mater. Sci. Technol. 26 (2010), https://doi.org/10.1016/S1005-0302(10)60064-3.
[29] X.H. Wang, Y.C. Zhou, High-temperature oxidation behavior of Ti_2AlC in air, Oxid. Met. 59 (2003) 303–320, https://doi.org/10.1023/A:1023092027697.
[30] B. Cui, D.D. Jayaseelan, W.E. Lee, Microstructural evolution during high-temperature oxidation of Ti_2AlC ceramics, Acta Mater. 59 (2011) 4116–4125, https://doi.org/10.1016/j.actamat.2011.03.035.
[31] X.H. Wang, Y.C. Zhou, Oxidation behavior of Ti_3AlC_2 at 1000–1400 °C in air, Corros. Sci. 45 (2003) 891–907, https://doi.org/10.1016/S0010-938X(02)00177-4.
[32] Z.J. Lin, M.S. Li, J.Y. Wang, Y.C. Zhou, High-temperature oxidation and hot corrosion of Cr_2AlC, Acta Mater. 55 (2007) 6182–6191, https://doi.org/10.1016/j.actamat.2007.07.024.
[33] S. Li, L. Xiao, G. Song, X. Wu, W.G. Sloof, S. van der Zwaag, Oxidation and crack healing behavior of a fine-grained Cr_2AlC ceramic, J. Am. Ceram. Soc. 96 (2013) 892–899, https://doi.org/10.1111/jace.12170.
[34] X. Lu, S. Li, W. Zhang, W. Yu, Y. Zhou, Thermal shock behavior of a nanolaminated ternary boride: MoAlB, Ceram. Int. (2018), https://doi.org/10.1016/j.ceramint.2018.08.071 in press.
[35] S.B. Li, H.L. Li, Y. Zhou, H.X. Zhai, Mechanism for abnormal thermal shock behavior of Cr_2AlC, J. Eur. Ceram. Soc. 34 (2014) 1083–1088, https://doi.org/10.1016/j.jeurceramsoc.2013.12.003.
[36] Measurement Standard of Ablation Properties of Materials, GJB323A-96, National Standard Committee of China, 1996.
[37] H. Li, S. Li, L. Zhang, Y. Zhou, Synthesis and ultra-high temperature ablation behavior of a ZrC/Cr_2AlC composite, Ceram. Int. 42 (2016) 5686–5692, https://doi.org/10.1016/j.ceramint.2015.12.095.
[38] J. Han, P. Hu, X. Zhang, S. Meng, W. Han, Oxidation-resistant ZrB_2–SiC composites at 2200 °C, Compos. Sci. Technol. 68 (2008) 799–806, https://doi.org/10.1016/j.compscitech.2007.08.017.
[39] C.W. Bale, P. Chartrand, S.A. Degterov, G. Eriksson, K. Hack, R. Ben Mahfoud, J. Melançon, A.D. Pelton, S. Petersen, FactSage thermochemical software and databases, Calphad 26 (2002) 189–228, https://doi.org/10.1016/j.calphad.2016.05.002.
[40] E.A. Gulbransen, K.F. Andrew, F.A. Brassart, Oxidation of Molybdenum 550 to 1700 °C, J. Electrochem. Soc. 110 (1963) 952–959, https://doi.org/10.1149/1.2425918.
[41] N. Floquet, O. Bertrand, J.J. Heizmann, Structural and morphological studies of the growth of MoO_3 scales during high-temperature oxidation of molybdenum, Oxid. Met. 37 (1992) 253–280, https://doi.org/10.1007/BF00665191.
[42] X. Zhang, P. Hu, J. Han, S. Meng, Ablation behavior of ZrB_2–SiC ultra high temperature ceramics under simulated atmospheric re-entry conditions, Compos. Sci. Technol. 68 (2008) 1718–1726, https://doi.org/10.1016/j.compscitech.2008.02.009.
[43] L. Xu, D. Zhu, Y. Liu, T.S. Suzuki, B. Kim, Y. Sakka, S. Grasso, C. Hu, Effect of texture on oxidation resistance of Ti_3AlC_2, J. Eur. Ceram. Soc. 38 (2018) 3417–3423, https://doi.org/10.1016/j.jeurceramsoc.2018.03.009.